CrossMark

Further realization of a flexible metamaterial-based antenna on indium nickel oxide polymerized palm fiber substrates for RF energy harvesting

Author for correspondence:
Taha A. Elwi, E-mail: taelwi82@gmail.com

Taha A. Elwi[1,2] and Ali M. Al-Saegh[3]

[1]Department of Communication Engineering, Al-Ma'moon University College, Baghdad, Iraq; [2]Electrical and Computer Engineering Campus, Long Island, NYiT University, USA and [3]Department of Computer Engineering Techniques, Al-Ma'moon University College, Baghdad, Iraq

Abstract

This paper discusses the design and fabrication of a low-profile Hilbert-shaped metamaterial (MTM) array-based antenna, forming a rectangular patch with partial ground plane backing; the rest is slotted with traces for RF energy harvesting. The antenna is mounted on a 28 mm × 32 mm indium nickel oxide polymerized palm fiber (INP) substrate and compared to the identical one based on FR4 substrate. The two prototypes are printed with silver nanoparticles. Numerical and experimental tests are applied to the antenna performance in terms of S_{11} and radiation patterns. The obtained antenna gain bandwidth product of the INP prototype is found to be significantly better than the FR4 prototype. The proposed INP antenna gain at 5.8 and 8 GHz frequencies is found to be about 4.56 and 7.38 dBi, respectively, while the FR4 antenna gain is found to be 4.56 and 6.85 dBi at 5.8 and 8 GHz, respectively. Finally, the resultant DC voltage and the efficiency of conversion from harvested RF energy are measured experimentally at 5.8 and 8 GHz for both proposed prototypes.

Introduction

Since microstrip patch antennas introduction in the 1950s, extensive investigations have been applied to them attributed to their distinguished features of conformability to mounting hosts and manufacturing ease, along with their low cost, light weight, and slim profiles [1]. The exhibition of the conventional microstrip antennas is limited to small bandwidth and moderate gain, which reduces their demands in modern UWB communication systems [2]. Recently, the frequencies of 3.1–10.6 GHz have been allocated for UWB applications by the Federal Communications Commission (FCC) [3]. A raised number of challenges has been done to overcome these limitations in performance and to allow return loss bandwidth of 10 dB over the entire band allocated for UWB applications. However, a large number of methods has been proposed to increase the bandwidth such as parasitic elements, multilayered patches, feed modifications, and aperture coupling [1, 4].

Recently, the performance of microstrip antennas has been enhanced with the introduction of metamaterial (MTM) structures [5–20]. For instance, split-ring resonator arrays were applied in printed circuit microwave devices for size reduction [5] with increasing the gain-bandwidth products [6]. Electromagnetic band gap structures were patterned either on the metal patches or etched from the ground plane as proposed in [7] and [8]. These structures show non-traditional properties, for example, negative permittivity and/or permeability, vanishing surface waves, and distinctive stopbands [8–10]. However, two core limitations that the resonant MTM structures suffer from are: the first is the narrow bandwidth over which the desired properties take place [11]; the second is the losses attributed to the conducting inclusions [12].

Miniaturized antennas made out of fractal-shaped space filling curves were proposed in [13–15] with enhanced bandwidth. A printed dipole mounted on a substrate of spiral MTM arrays backed with a truncated defected ground plane was proposed for wearable applications [16]. In [17], a meander structure was coupled with split-ring resonator arrays to realize printed RFID tags. A spiral-shaped antenna was printed on a substrate containing MTM inclusions in [18] to enhance the radiation properties over X and Ku bands. A multi-resonant fractal MTM antenna based on a CPW excitation was developed in [19]. A rectangular MTM array patch mounted on a substrate layer of a defected ground plane was invented in [20] for UWB applications.

In this paper, a new microstrip antenna design is presented for RF energy harvesting applications. The antenna provides an enhanced gain bandwidth product over the Wi-Fi, WLAN, and WiMax frequency bands. Basically, the patch structure of the proposed antenna is a fractal Hilbert curve MTM backed by slots. Extensive numerical investigations are reported to
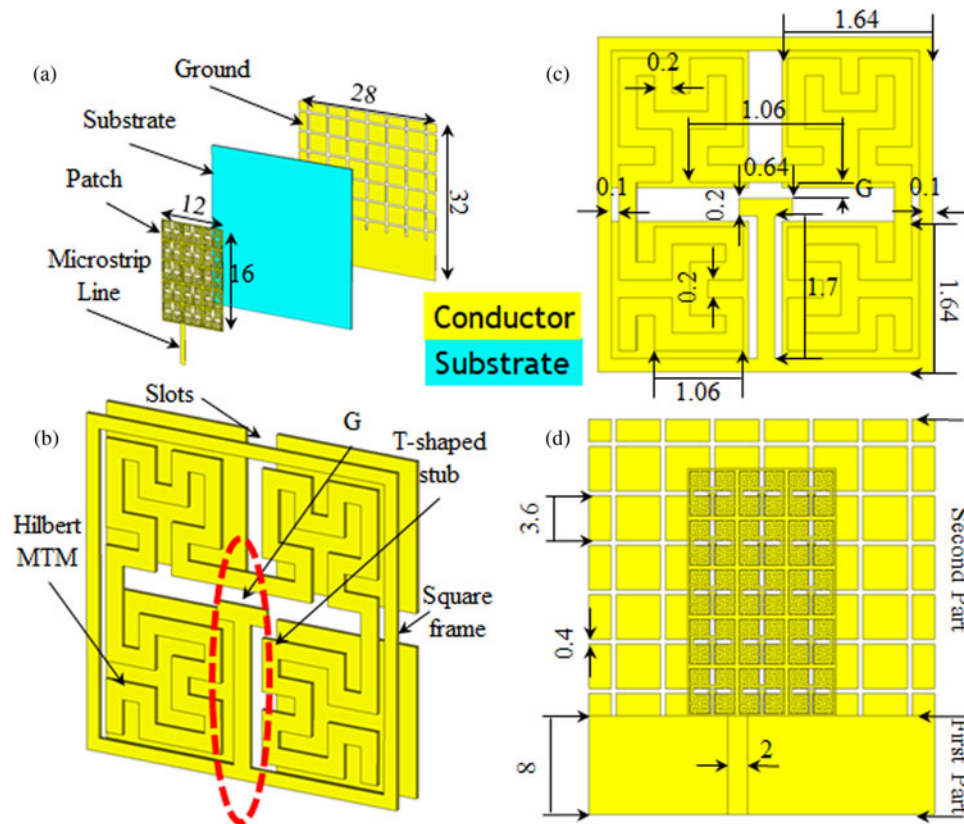
CAMBRIDGE
UNIVERSITY PRESS

Fig. 1. Antenna geometry; (a) 3-D decomposed view, (b) MTM unit cell 3-D view, (c) MTM unit cell front view, and (d) antenna front view. All dimensions are in mm scale.

illustrate the design methodology and performance of the proposed antenna. Two prototypes are constructed from silver nanoparticles (SNP) on indium nickel oxide polymerized palm fiber (INP) and FR4 substrates to be tested and compared against each other. The antenna conversion efficiency and measured output DC voltage are evaluated for the two fabricated prototypes.

Antenna geometry

The proposed antenna configuration is presented in Fig. 1. The patch consists of 3×5 array planar Hilbert elements that are printed on 0.8 mm thickness FR4 and INP substrates. The patch and ground plane are printed with SNP as a conductor as presented in Fig. 1(a). The dielectric constant and losses are $\varepsilon_r = 4.4$ and $\tan\delta = 0.02$, respectively, for the FR4 substrate, while $\varepsilon_r = 3.106$ and $\tan\delta_E = 0.045$ and $\mu_r = 1.548$ and $\tan\delta_H = 0.13$ for the INP substrate. The proposed fractal geometry is considered to increase the unit-cell electrical length within an area of $4 \times 4 \, \text{mm}^2$ and to control the input impedance matching at the desired resonant frequencies through capacitive coupling using the T-shaped stub as seen in Fig. 1(a). The energy is capacitively coupled to the Hilbert MTM from the T-shaped stub through a gap distance (G) as shown in Fig. 1(b). Moreover, the unit cell provides small shadowing area that is essential for self-powered wireless devices [21]. To ensure that the driving current excites the Hilbert MTM through capacitive coupling (Fig. 1(b)), a square conductive frame is proposed to surround each unit cell separately. The other geometrical details of the MTM unit cell are presented in Fig. 1(c). The patch is excited with $50\,\Omega$ off-centered

transmission line of 2 mm width and 8 mm length as depicted in Fig. 1(d). The combined effect of ground plane slots and MTM unit cells is evident in the shape of the radiation pattern, which exhibits a linear electric polarization (corresponding to the E-plane) parallel to antenna's plane [21]. The rest of the ground plane is defected with a 7×6 periodically etched slots as shown in Fig. 1(d). The partial ground plane width is adjusted to maximize the antenna bandwidth as explained in [22].

The elementary radiator is inspired by the approach outlined in [13]; different Hilbert orders were presented to achieve an MTM structure with direction-dependent band gap. In this paper, a patch structure based on Hilbert unit cell of the third order is proposed. The width of the Hilbert line is selected so as not to cause undesired crossing between the printed traces because of the limited resolution of the printing and etching processes.

Design methodology

In this section, the author offers the procedure followed to arrive at the final design given in Fig. 1. This section also is intended to explain the antenna operation mechanisms based on simulations conducted using CST MWS (www.cst.com). The design starts with a solid rectangular patch, case 1, backed with partial ground plane as presented in Fig. 2(a). In case 2, the solid patch is reformed to 3×5 etched square array as seen in Fig. 2(b). Further, a Hilbert conductor pattern, which makes the current antenna design different from the approach reported in [20], is introduced inside the fishnet geometry as seen in Fig. 2(c) and is referred to as case 3. The geometrical details are summarized in Table 1.
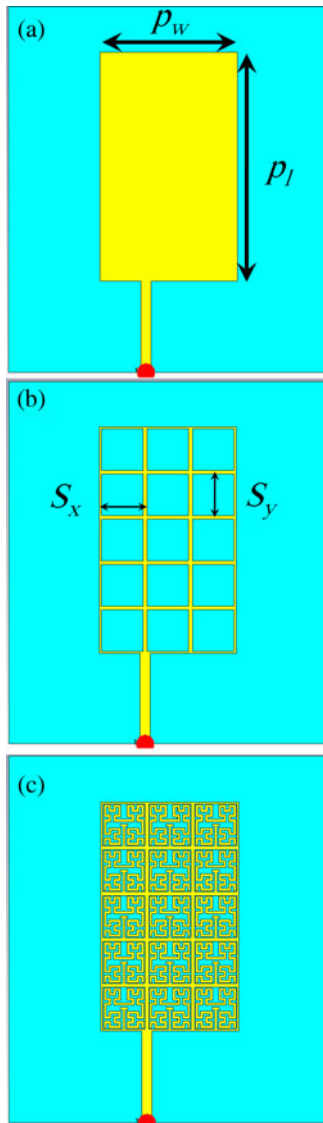
Fig. 2. Numerical model of the proposed cases; (a) case 1, (b) case 2, and (c) case 3.

Table 1. Antenna geometrical details

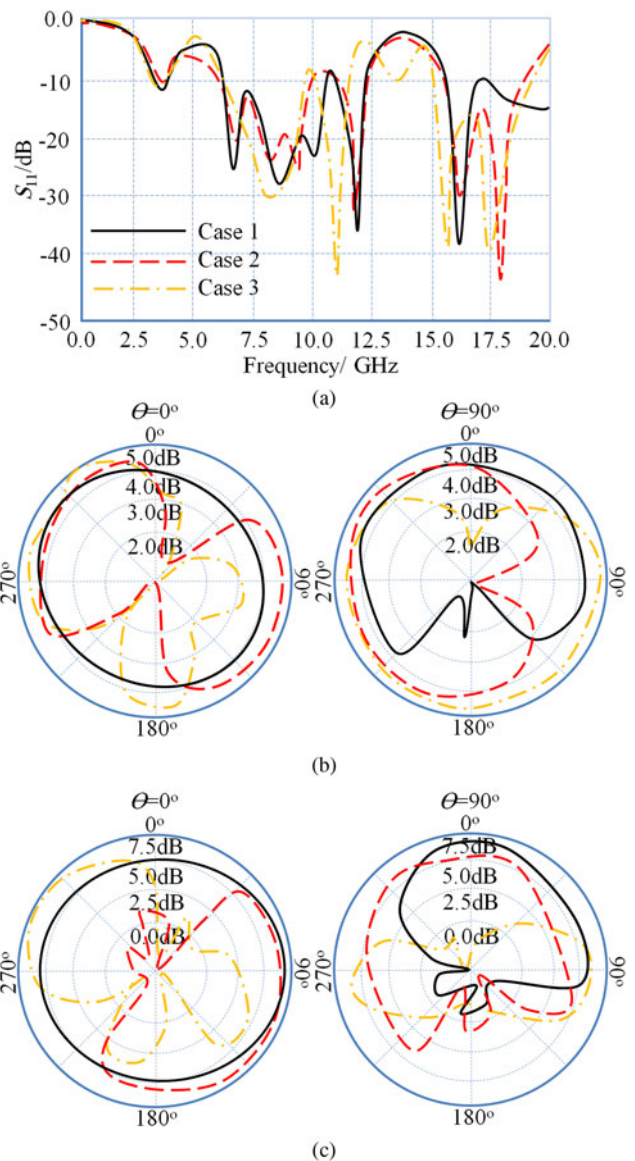| Dimensions	Value/mm
Slot length (S_y)	3.68
Slot width (S_x)	3.68
Patch length (p_l)	20
Patch width (p_w)	12

Fig. 3. Antenna performance in terms of S_{11} spectra for all cases in (a) and 2-D radiation patterns at 5.8 GHz in (b) and at 8 GHz in (c).

Design development

The S_{11} spectra evaluated from CST MWS are presented in Fig. 3. It is found that the partial ground plane that is introduced in all cases has a significant impact on bandwidth enhancement. Such results agree with many published results in the literature [12]. The patch shape change affects the antenna radiation patterns. For example, the 3-D radiation patterns are evaluated at 5.8 GHz, where the antenna possesses excellent matching. In general, the antenna radiation patterns are found to be mostly directed to the side directions as seen in Fig. 4.

MTM principles of operation

In this section, the operations of the MTM and the ground plane slots of the proposed work are discussed. As seen in Fig. 3(d), the radiation pattern is significantly affected by the introduction of the MTM structure. In general, the antenna radiation patterns are found to be tangential to the patch surface instead of being broadside radiation patterns as in traditional microstrip antennas

[1]. This can be probably understood from the surface current distribution that is presented in Fig. 4(a), in which the current distribution is mainly concentrated on the patch width (p_w) due to the low impedance in comparison to the impedance along the patch length (p_l). Hence, the number of unit cells along p_w is 3 and along p_l is 5. If we treat each unit cell as impedance, this realizes surface impedance along p_l higher than the
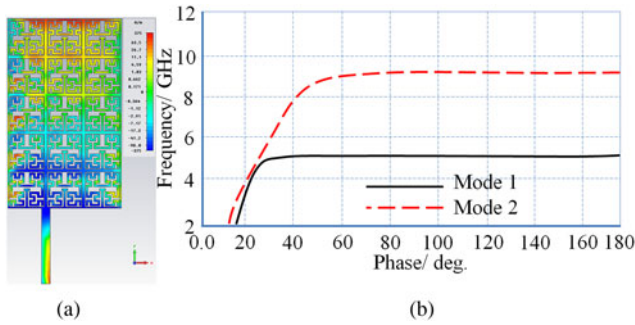
Fig. 4. In (a) current distributions and (b) dispersion diagram.

impedance along p_w by a ratio of 5/3. For this, the antenna radiation is mainly directed parallel to the patch length. The ground plane defects with the periodical slots are responsible for lowering the antenna quality factor [16] that increases the bandwidth. As seen in Fig. 4(b), the proposed MTM shows a band gap from 5 to 9 GHz based on the INP substrate as seen in Fig. 4(b).

Bandwidth

To specify the effect of the coupling gap (G) that is shown in Fig. 1(b), S_{11} spectra for three different gaps: 0.05, 0.1, and 0.15 mm, are evaluated and presented in Fig. 5. A significant effect of G variation is found on the resonance value, return loss magnitude, and bandwidth. As the G value increases, the bandwidth increases with noticeable degradations in the return loss values. Hence, the G value is considered to be 0.15 mm. An observable effect is found in the antenna matching by changing the length insets of T-shaped stubs inside the Hilbert-shaped unit radiators.

The design of the slotted ground dimensions (S_w) is discussed here. In spite of the major utility of UWB applications, the antenna bandwidth enhancement is analyzed. Figure 6 shows the change in the S_{11} spectra with varying slot lines width. This explains the correlative effects of the slot width on the antenna coupling. Moreover, such slots exhibit low spurious feed radiations leakage with matching capacitance at resonating frequencies [12]. An array of capacitor–inductor (C–L) resonators of parallel branches is modeled to stimulate the effects of the electromagnetic fringing and leakage from the conducted slots [13]. The values of the C–L branches are relatively affected by the constitutive electromagnetic properties of the substrate ε_r and μ_r. Moreover, the physical dimensions S_x, ε_r, S_w, and substrate height (h) are directly related to the value of equivalent C–L branches [13] as:

$$C = \frac{p_w \varepsilon_o (1 + \varepsilon_r)}{\pi} \cosh^{-1}\left(\frac{h + 2S_w}{S_w}\right) \tag{1}$$

$$L = \mu_o \mu_r p_l \tag{2}$$

$$BW = \frac{1}{\eta}\sqrt{\frac{L}{C}}. \tag{3}$$

These equations describe the slots response in terms of bandwidth analytically. Such slots array supports degenerative coupling reduction, which increases the antenna bandwidth significantly as
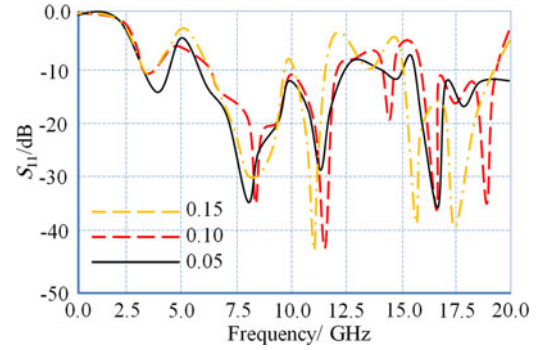

Fig. 5. S_{11} spectra change with respect to G variation.
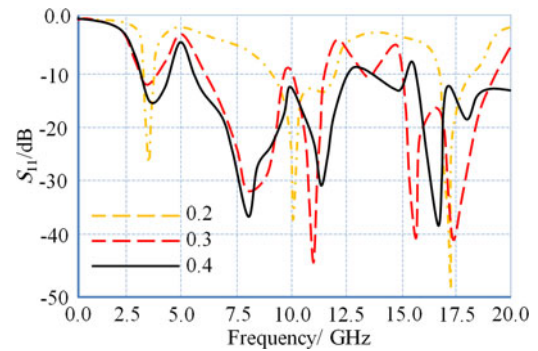

Fig. 6. S_{11} spectra change with respect to S_w change.

shown in Fig. 6. As explained earlier, the distribution of the current is mainly concentered at the patch width over the patch length to realize a high p_l/p_w ratio which is relatively proportional to the L/C ratio. In such a case, the introduction of the ground plane defects is justified by increasing the antenna bandwidth through reducing the quality factor [16]. This also can be explained through two orthogonal field components that are generated along the patch width and length [11] which relatively increases the ratio of p_l/p_w.

Antenna printing process

The proposed antenna prototypes are manufactured with DMP 2800 material printer as seen in Fig. 7. The nominal drop volume from the printer cartridge is fixed to 10 pl. The cartridge is connected to a piezo-electric head through 16 jets. The INP and FR4 substrates are mounted on the printer heated platen. The platen temperature is raised up to 60°C. To realize a qualified printout, a single ink jet is used with 20 mV pump pressure-driven device. Moreover, the printer head is adjusted to 0.5 mm height from the substrate to avoid ink stream flaring. The same geometry is printed out with five layers and 20 s delay between each consecutive pass to ensure continuous traces. Finally, the annealing process for resulted printouts is conducted at 120°C inside LPKF oven for 10 h. The 50 Ω SMA port is connected to the prototypes using silver paste.

The electrical conductivity of the printout is measured first for FR4 prototype which is found to be $8.8 \pm 0.2 \times 10^4$ S/m. However, the electrical conductivity is increased up to $9.2 \pm 0.2 \times 10^4$ S/m when the same structure is printed on the INP substrate. Such
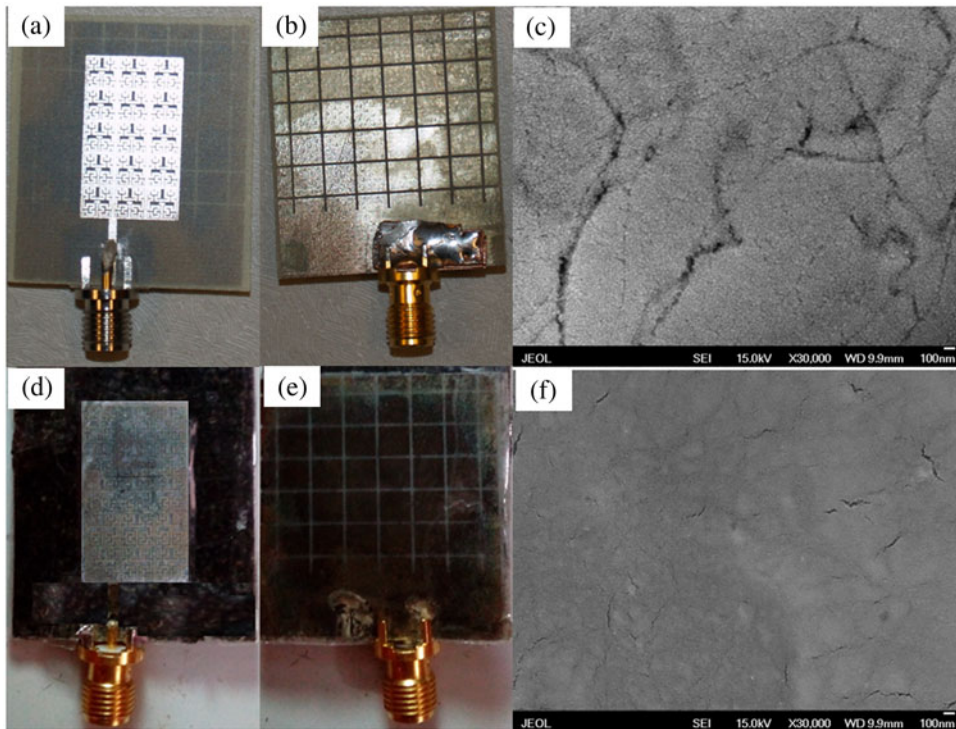
Fig. 7. Fabricated prototypes; (a) and (b) for the FR4 substrate, while (d) and (e) for the INP substrate. The SEM images for the print out on the FR4 and INP substrates are shown in (c) and (f), respectively.

conductivity enhancement is attributed to the substrate surface viscosity and smoothness that offer continuous clear printing conductions as can be seen in the SEM images presented in Figs 7(c) and 7(f) for the proposed print out. The top cross-sectional SEM view for the print out on the FR4 substrate shows large crakes that hinder the electron motion in comparison to the print out on the INP substrate. The values of the measured conductivity are used for CST MWS and HFSS simulations.

Antenna performance measurements

Antenna performance under flat conditions

The antenna performance is tested numerically using HFSS software package (www.ansoft.com) based on the finite element method. The fabricated prototypes are measured and compared to each other against numerical simulations as shown in Fig. 8. The simulated S_{11} spectra for INP and FR4 prototypes show reasonable agreement with the measurement results as shown in Figs 8(a) and 8(b), respectively. Moreover, the INP prototype bandwidth shows a wider than the one based on FR4 substrate with better matching impedance. The proposed antenna radiation patterns are measured at 5.8 GHz for both prototypes as seen in Figs 8(c) and 8(d) in the E- and H-planes. It is found that the proposed antenna-based INP substrate shows the same gain, about 4.56 dBi, with that of the fabricated-based FR4 substrate. The antenna radiation patterns are measured at 8 GHz as seen in Figs 8(e) and 8(f). It can be revealed that the proposed antenna-based INP substrate shows a gain of 7.38 dBi, while the one based on FR4 substrate is about 6.85 dBi. Such enhancement in the gain is attributed to the radiation focusing when the antenna is mounted on the INP substrate. In general, the measured radiation

patterns of both prototypes at 5.8 and 8 GHz are found almost to show identical profiles; thus, changing the substrate type has no impact on the surface current distribution on the antenna patch.

Antenna performance under bending conditions

To realize the antenna performance as a flexible structure, the experimental measurements are extended by bending the antennas on two different angles: 10° and 20°. The bended prototypes are measured and compared against their flat profiles as seen in Fig. 9. The measured S_{11} spectra for the FR4 prototype show a significant degradation in the matching magnitude as seen in Fig. 9(a). However, for the INP prototype in flat case, the S_{11} spectrum is found to be unaffected significantly with bending as depicted in Fig. 9(b). The bended antennas radiation patterns in the E- and H-planes are measured at 5.8 and 8 GHz in comparison to the flat case as seen in Figs 9(c)–9(f). The FR4 prototype gain, at 5.8 GHz, is changed from 4.5 dBi for the flat case to 3.7 dBi than 2.9 dBi, respectively, when it is bended at 10° and 20° as seen in Fig. 9(c). A sever gain degradation is observed in the FR4 prototype, at 8 GHz, from 6.85 dBi for the flat case to 2.1 and 1.5 dBi when it is bended at 10° and 20°, respectively. This is attributed to the side lobes significance after antenna bending. However, the antenna radiation patterns for the INP prototype are mostly unaffected as seen in Figs 9(e) and 9(f). Therefore, the gain of the INP prototype is insignificantly degraded: for example, at 5.8 GHz, the gain for the INP prototype remains almost around 4.5 dBi for both angles of bending. Also, the INP prototype gain at 8 GHz is found to vary from 7.38 dBi for the flat case to 6.5 and 6 dBi when it is bended at 10° and 20°, respectively. This is attributed to the magnetic field storing inside the
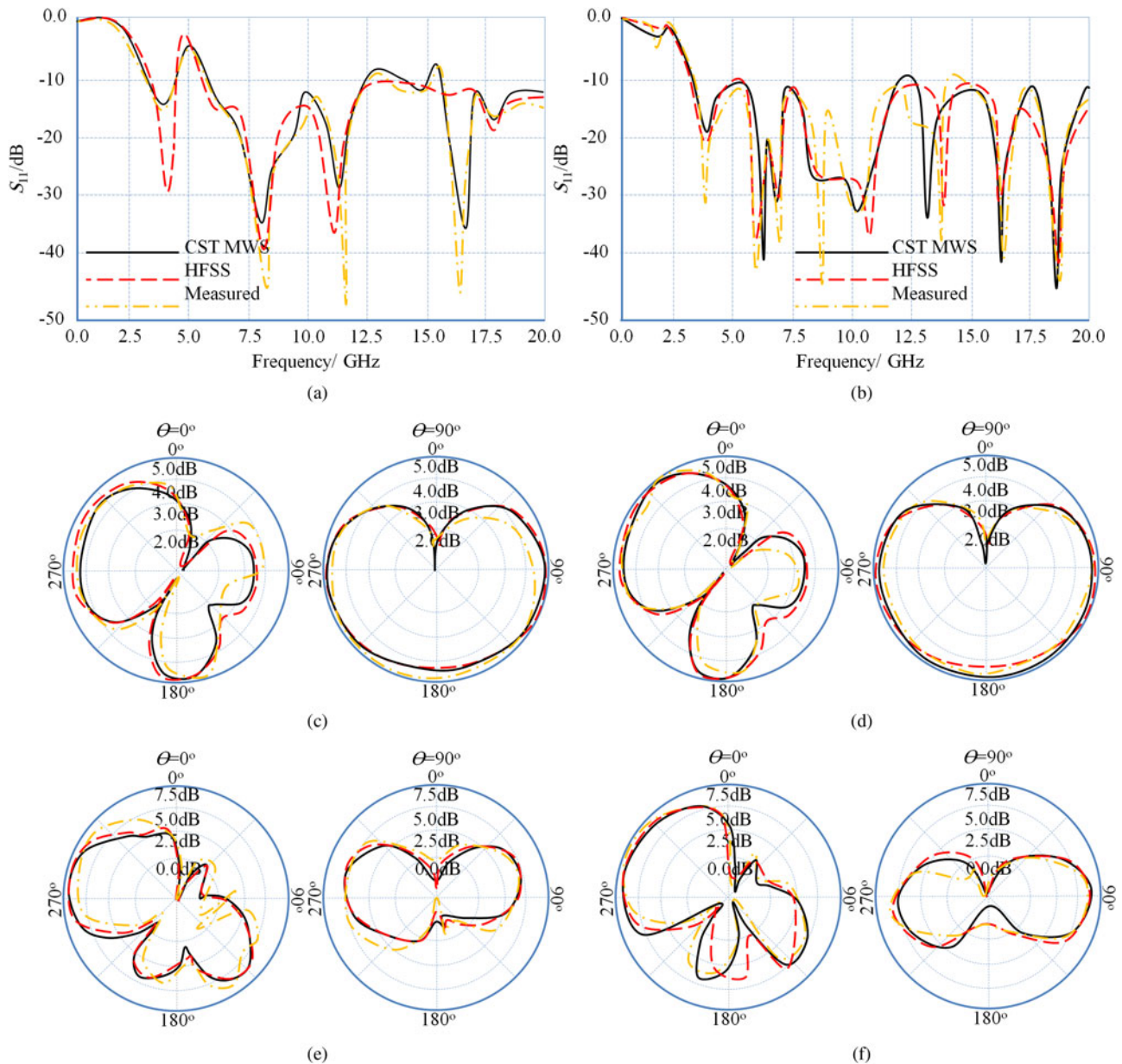
Fig. 8. Measured antenna performance in comparison to the simulated results; (a) S_{11} based on FR4 prototype, (b) S_{11} based on INP prototype, (c) radiation patterns at 5.8 GHz based on FR4 prototype, (d) radiation patterns at 5.8 GHz based on INP prototype, (e) radiation patterns at 8 GHz based on FR4 prototype, and (f) radiation patterns at 8 GHz based on INP prototype.

INP substrate due to the μ_r component [5]. Therefore, the radiation patterns of the INP prototype are found almost unaffected with bending.

The performance of the proposed prototypes is compared and summarized in Table 2. From the obtained results, the INP prototype shows excellent immunity against bending effects in comparison to the one based on FR4 substrate that is attributed to μ_r component of the INP substrate [14]. In another word, the advantage in using INP material is the magnetic field energy can be stored in the INP substrate to help the antenna to radiate regardless the value of the bending angle [20].

RF energy harvesting

Now, the harvested RF energy at 5.8 and 8 GHz of the proposed antenna-based INP and FR4 substrate prototypes is discussed

here. In Fig. 10, the RF harvester of 7 capacitor-based Schottky diodes Villard voltage doubler stages is presented. The chemical etching process is used to manufacture the proposed circuit on Fiberglass Reinforced Epoxy board of 2 mm thickness and ε_r of 3.9. Two SMA ports of 50 Ω input/output matching impedance are connected to the fabricated circuit. The manufactured circuit area is 100×40 mm^2. A matching load is attached close to the RF_{input} port to maximize the antenna coupling to the RF harvester [17]. The chock circuit is presented to the RF circuit to reduce the ripple factor in the output DC voltage [18].

The measured output DC voltage is realized using a UWB stander horn antenna at 5.8 and 8 GHz with a bore-sight gain of 16 and 22 dBi, respectively. The DC voltage is screened on a digital oscilloscope as presented in Fig. 11(a) for both proposed prototypes at 5.8 GHz. It is found that the proposed antenna-
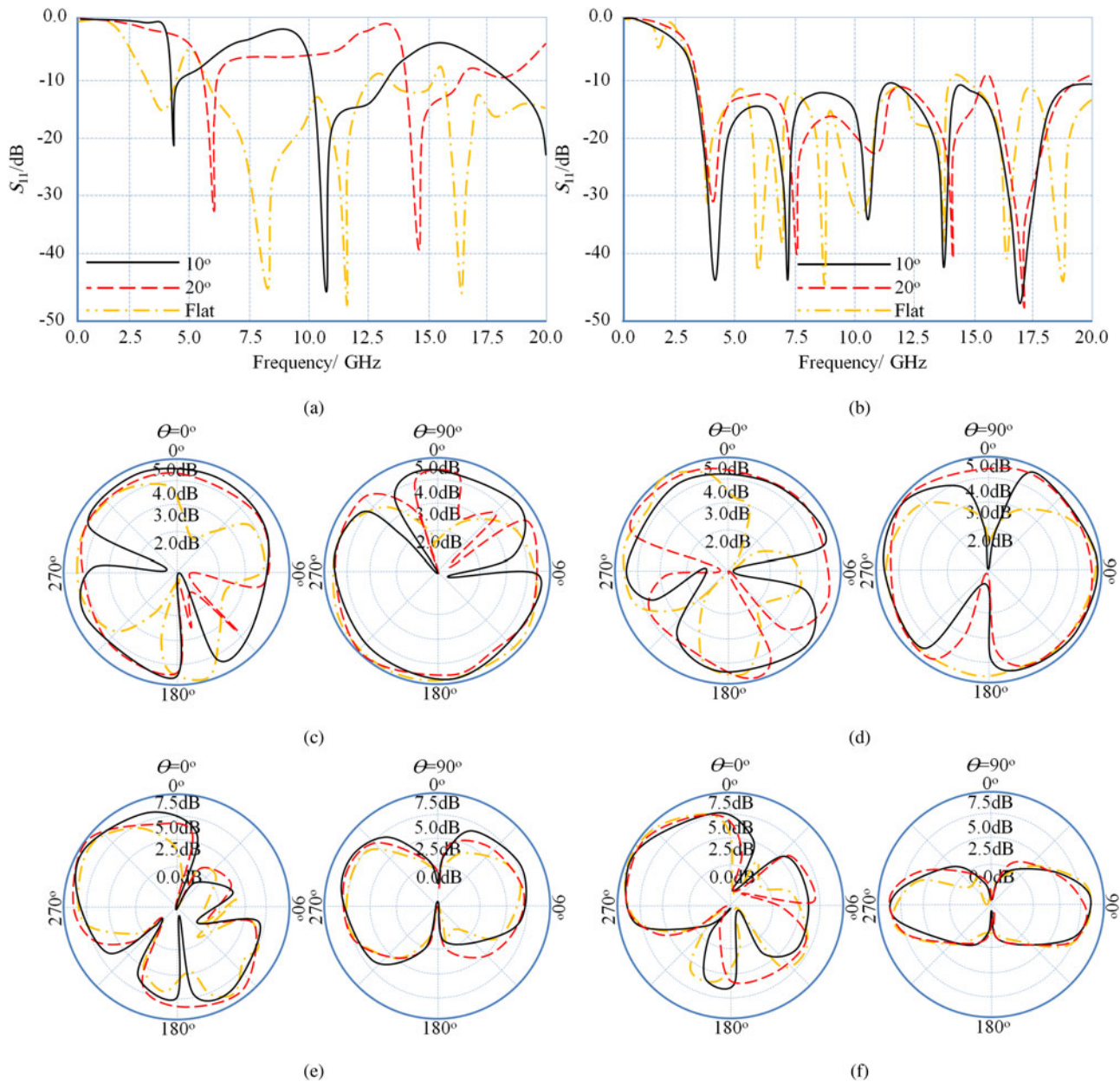
Fig. 9. Antenna performance with bending effects; (a) and (b) S_{11} spectra with FR4 and INP, respectively. (c) and (d) Radiation patterns at 5.8 and 8 GHz, respectively, with FR4. (e) and (f) Radiation patterns at 5.8 and 8 GHz, respectively, with INP.

Table 2. Antenna performance comparison between the proposed cases

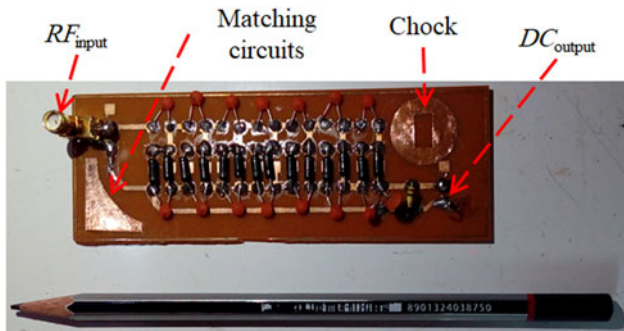| Substrate	Performance		Flat	10°	20°
INP	Bandwidth/GHz at $S_{11}<-10$ dB		3.1–20	3–20	3–20
	Gain/dBi	5.8 GHz	4.56	4.5	4.5
		8 GHz	7.38	6.5	6
FR4	Bandwidth/GHz at $S_{11}<-10$ dB		5.7–12.5	10–13	14–16.5
	Gain/dBi	5.8 GHz	4.56	3.7	2.9
		8 GHz	6.85	2.1	1.5

Fig. 10. RF energy harvester circuit prototype.

based INP substrate shows almost a better enhancement in the output DC voltage from the one based on the FR4 substrate. Nevertheless, the conversion efficiency at 5.8 GHz of the antenna based on the INP substrate is found to be enhanced further more than the one based on the FR4 substrate as depicted in Fig. 11(b). The conversion efficiency is obtained with respect to the power

transmitted from the RF source. The same measurements at the output DC voltage and the conversion efficiency are repeated at 8 GHz, to end up with the same previous conclusion. From measurements, the maximum output DC voltage is about 2.98 mV at 5.8 GHz with conversion efficiency of 98% for the INP prototype, while the same prototype is found to provide a maximum output DC voltage of 2.76 mV at 8 GHz with conversion efficiency of 96%.

In Table 3, a comparison study is provided between the proposed antenna and other published results. Consequently, it can be claimed that the proposed antenna shows superior achievements compared to those published in the literature.

Conclusion

In this paper, a miniaturized MTM-based printed antenna circuitry of enhanced gain bandwidth product is presented. The MTM is structured from a Hilbert-shaped unit cell mounted on a flexible INP substrate backed with partial ground plane defected with periodical slots. The same antenna geometry is mounted on the FR4 substrate for comparison. After testing the proposed
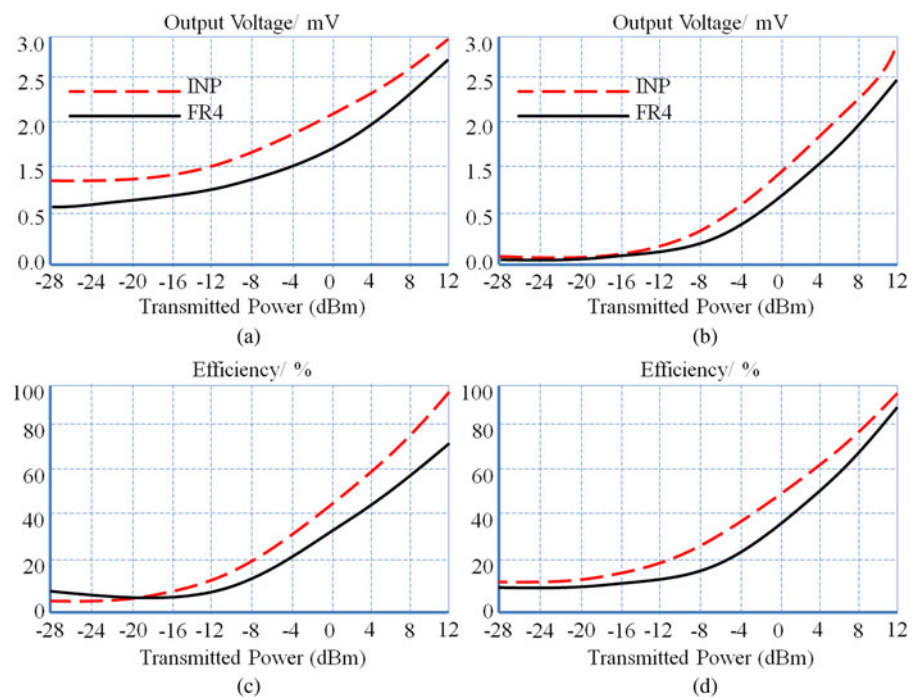

Fig. 11. RF energy harvesting measurements: (a) output DC voltage at 5.8 GHz, (b) conversion efficiency at 5.8 GHz, (c) output DC voltage at 8 GHz, (b) conversion efficiency at 8 GHz.

Table 3. Comparison of the proposed antenna validation

Ref.	Size/mm^3	Freq./GHz	Gain/dBi	Eff.
[4]	14.2 × 6.32 × 0.8	2.45	2.3	62%
[7]	19.2 × 6.32 × 0.8	5.8	2.8	70%
[18]	30 × 22 × 0.8	2.45, 5.8	4.4, 5.1	83%
[19]	105.5 × 93 × 5	3.1	4.8	80%
[20]	50 × 50 × 1.6	2.45, 5.8	3.5, 4.3	78%, 83%
Work	20 × 12 × 2	5.8, 8	4.5, 7.38	98%, 96%

antennas performance, it is found that the INP antenna shows an enhanced gain bandwidth product in comparison to the identical one based on FR4 substrate. Such enhancement is attributed to the permeability component of the proposed INP substrate. A good agreement is found between the measured and simulated antenna performance for both proposed prototypes. The experimental measurements are extended to evaluate the harvested RF energy based on the collected output DC voltage and conversion efficiency. The effect of bending is studied and it is found that the performance of the prototype-based INP substrate is more immune variation than the one based on FR4 substrate. Finally, it is found that the INP prototype provides an output DC voltage of about 2.98 mV and conversion efficiency of 98% at 5.8 GHz, while the maximum output DC voltage is 2.76 mV with conversion efficiency of 96% at 8 GHz.

References

1. **Balanis CA** (2006) *Antenna Theory: Analysis and Design*. John Wiley & Sons.
2. **Bancroft R** (2004) *Microstrip and Printed Antenna Design*. Raleigh, NC, USA: Noble Publishing.
3. **Elwi TA** (2018) Metamaterial based a printed monopole antenna for sensing applications. *International Journal of RF and Microwave Computer-Aided Engineering* **28**, 1–10.
4. **Elwi TA** (2019) Novel UWB printed metamaterial microstrip antenna based organic substrates for RF-energy harvesting applications. *AEU – International Journal of Electronics and Communications* **101**, 1–10.
5. **Elwi TA and Ahmed BA** (2018) A fractal metamaterial based printed dipoles on a nickel oxide polymer palm fiber substrate for Wi-Fi applications. *AEU – International Journal of Electronics and Communications* **96**, 122–129.
6. **Elwi TA** (2018) A miniaturized folded antenna array for MIMO applications. *Wireless Personal Communications* **98**, 1–24.
7. **Elwi TA, Tawfeeq O-A, Alnaiemy Y, Ahmed HS and Lajos N** (2018) An UWB monopole antenna design based RF energy harvesting technology. *IEEE 3rd Scientific Conference of Electrical Engineering SCEE 2018*, December, 2018.
8. **Engheta N and Ziolkowski RW** (2007) *Electromagnetic Metamaterials: Physics and Engineering Explorations*. Rosewood drive danvers, MA, USA: John Wiley & Sons.
9. **Cui TJ, Smith D and Liu R** (2003) *Metamaterials: Theory, Design, and Applications*. New York, NY, USA: John Wiley & Sons.
10. **Elwi TA, Hamed MM, Abbas Z and Elwi MA** (2014) On the performance of the 2D planar metamaterial structure. *International Journal of Electronics and Communications* **68**, 846–850.
11. **Sievenpiper D, Zhang L, Jimenez Broas RF, Alexopolous NG and Yablonovitch E** (1999) High-impedance electromagnetic surfaces with a forbidden frequency band. *IEEE Transactions on Microwave Theory and Techniques* **47**, 2059–2074.
12. **Clavijo S, Diaz RE and McKinzie WE** (2003) Design methodology for Sievenpiper high-impedance surfaces: an artificial magnetic conductor for positive gain electrically small antennas. *IEEE Transactions on Antennas and Propagation* **51**, 2678–2690.
13. **Elwi TA** (2018) A slotted lotus shaped microstrip antenna based an EBG structure. *Journal of Material Sciences & Engineering* **7**, 1–15.
14. **Ziolkowski RW and Erentok A** (2006) Metamaterial-based efficient electrically small antennas. *IEEE Transactions on Antennas and Propagation* **54**, 2113–2130.
15. **Ziolkowski RW and Erentok A** (2005) At and beyond the Chu limit: passive and active broad bandwidth metamaterial-based efficient electrically small antennas. *IEE Proceeding* **1**, 116–128.
16. **Palandoken M, Grede A and Henke H** (2009) Broadband microstrip antenna with left-handed metamaterials. *IEEE Transactions on Antennas and Propagation* **57**, 331–338.
17. **Elwi TA** (2017) Electromagnetic band gap structures based an ultra-wideband microstrip antenna. *Microwave and Optical Letters* **59**, 827–834.
18. **Takacs A, Aubert H, Fredon S, Despoisse L and Blondeaux H** (2014) Microwave power harvesting for satellite health monitoring. *IEEE Transactions on Microwave Theory and Techniques* **62**, 1090–1098.
19. **Elwi TA, AL-Hussain ZA and Tawfeeq O** (2019) Hilbert metamaterial printed antenna based on organic substrates for energy harvesting. *IET Microwaves, Antennas & Propagation* **12**, 1–8.
20. **Elwi TA, Jassim DA and Mohammed HH** (2020) Novel miniaturized folded UWB microstrip antenna-based metamaterial for RF energy harvesting. *International Journal of Communication Systems* **1**, 1–15.
21. **Imran AI and Elwi TA** (2017) A cylindrical wideband slotted patch antenna loaded with frequency selective surface for MRI applications. *Engineering Science and Technology, an International Journal* **20**, 990–996.
22. **Al-Sabbagh HM, Elwi TA, Al-Naiemy Y and Al-Rizzo HM** (2019) A compact triple-band metamaterial-inspired antenna for wearable applications. *Microwave and Optical Technology Letters* **11**, 1–15.

Taha A. Elwi received his B.Sc. degree in the electrical engineering department (2003) (Highest Graduation Award), Postgraduate M.Sc. degree in laser and optoelectronics engineering department (2005) (Highest Graduation Award) from Nahrain University Baghdad, Iraq. From April 2005 to August 2007, he was working with Huawei Technologies Company, Baghdad, Iraq. On January 2008, he joined the University of Arkansas at Little Rock and he obtained his Ph.D. degree in December 2011 from the system engineering and science department. His research areas include wearable and implantable antennas for biomedical wireless systems, smart antennas, Wi-Fi deployment, electromagnetic wave scattering by complex objects, design, modeling and testing of metamaterial structures for microwave applications, design, and analysis of microstrip antennas for mobile radio systems, precipitation effects on terrestrial and satellite frequency re-use communication systems, effects of the complex media on electromagnetic propagation and GPS. The nano-scale structures in the entire electromagnetic spectrum are a part of his research interest.

Ali M. Al-Saegh received his B.Sc. degree in electronic and communications (2005), and M.Sc. degree in satellite engineering (2008) from electronic and communications engineering department in Nahrain University, Baghdad, Iraq. He received his Ph.D. degree in wireless communications engineering from computer and communication system engineering department in Universiti Putra Malaysia (UPM), Selangor, Malaysia, in 2015. From 2009 to 2012, he was attached as a lecturer in computer engineering techniques and communications engineering departments in Al-Ma'moon university college, Iraq. From 2012 to 2013, he was a research assistant in the department of computer and communication systems engineering, UPM, Malaysia. Since 2015, he has been a senior lecturer in computer engineering techniques department in Al-Ma'moon university college, Iraq. His areas of specialization are radio waves propagation, satellite communications, atmospheric impairments prediction, channel modeling, mitigation techniques, multimedia transmission, and resource management.